Physics of the Earth and Planetary Interiors xxx (2010) xxx–xxx

Contents lists available at ScienceDirect

Physics of the Earth and Planetary Interiors

journal homepage: www.elsevier.com/locate/pepi

A stabilization algorithm for geodynamic numerical simulations with a free surface

Boris J.P. Kaus [a,b,*], Hans Mühlhaus [c], Dave A. May [a]

[a] Geophysical Fluid Dynamics, Department of Earth Sciences, ETH Zurich, Switzerland
[b] University of Southern California, Los Angeles, USA
[c] ESCC, University of Queensland, Australia

ARTICLE INFO

Article history:
Received 14 December 2009
Received in revised form 1 April 2010
Accepted 16 April 2010

Edited by: M. Jellinek.

Keywords:
Lithospheric deformation
Rheology
Stress state
Numerical modelling
Free surface
Computational geodynamics

ABSTRACT

Geodynamic processes are in many cases coupled to surface processes such as erosion of mountains or deposition of sediments in basins. Numerical models that study the effect of such surface processes on the dynamics of the lithosphere use either a self-consistent free surface approach or approximate it by adding a weak, low density "air" layer on top of the model domain. A main problem with such setups, however, is that they are numerically unstable, which is caused by the fact that the density difference that drives geodynamic processes (~30–100 kg/m^3) is much smaller than the density difference between rocks and air (~3000 kg/m^3). In order to retain isostatic balance, one should thus employ a time step that is at least 30 times smaller than in models with a free slip upper boundary condition, which makes such models computationally very expensive.

Here we describe a new free surface stabilization approach (FSSA) that largely overcomes this time step restriction. In this work, we apply the stabilization technique to consistent free surface models utilizing a finite element discretization. The approach is based on the observation that most geodynamical simulations perform time-dependent simulations by solving the static Stokes equations and then updating the material or temperature fields in a separate step. If, however, the time-dependency of these quantities is taken into account during the discretization of the momentum equations, additional surface traction terms appear in the weak form of the FE formulation. These terms, which depend on the employed time step and velocity, essentially correct for the change of forces in an element due to advection or distortion of every element. By time-discretizing them, they act as a stabilizing term that largely increases the time steps that can be employed (by a factor 20–100 depending on the time stepping criteria that is used).

We illustrate the accuracy and power of this method with examples of a free surface Rayleigh–Taylor instability and with a free subduction experiment.

1. Introduction

Recently, there has been an increased interest in understanding the interactions between surface processes and deep tectonic processes (e.g., Braun, 2006; Braun and Yamato, in press; Kaus et al., 2008; Willett, 1999). In order to model the interaction between such processes in a self-consistent manner, one has to take the free surface of the Earth into account. In the past, the free surface of the Earth was incorporated into mantle convection codes by adding a surface traction on the upper (undeformable) boundary (e.g., Gurnis et al., 1996; Zhong et al., 1996). Whereas such models give important insights and probably capture the first order, long wavelength, picture of mantle–surface interaction (Poliakov and Podladchikov, 1992), there are cases in which this is not sufficient. Examples include models of coupled sedimentation and erosion in a deforming fold-and-thrust belt (Simpson, 2006), as well as a benchmark study on free subduction (Schmeling et al., 2008).

Particularly, this last study pointed out the potential importance of a free surface on slab dynamics. One of the purposes of the study was to reproduce laboratory experiments on free subduction in which a viscous slab sinks into a viscous mantle. Whereas laboratory experiments show slab bending and unbending, numerical experiments with a free slip boundary condition develop a dripping instability (Fig. 1). If a free surface boundary condition is employed instead, or if a "sticky air" layer is taken into account, the numerical models behave fairly similar to laboratory experiments (see Fig. 1 for an example).

Both approaches, however, pose severe restrictions on the computational time step. The simulation with free slip upper boundary condition of Fig. 1, for example, was done with an average time step

* Corresponding author at: Geophysical Fluid Dynamics, Department of Earth Sciences, ETH Zentrum, Sonnegstrasse 5, 8092 Zurich, Switzerland.
Tel.: +41 44 633 7539; fax: +41 44 633 1065.
E-mail address: kaus@erdw.ethz.ch (B.J.P. Kaus).

0031-9201/$ – see front matter © 2010 Published by Elsevier B.V.
doi:10.1016/j.pepi.2010.04.007

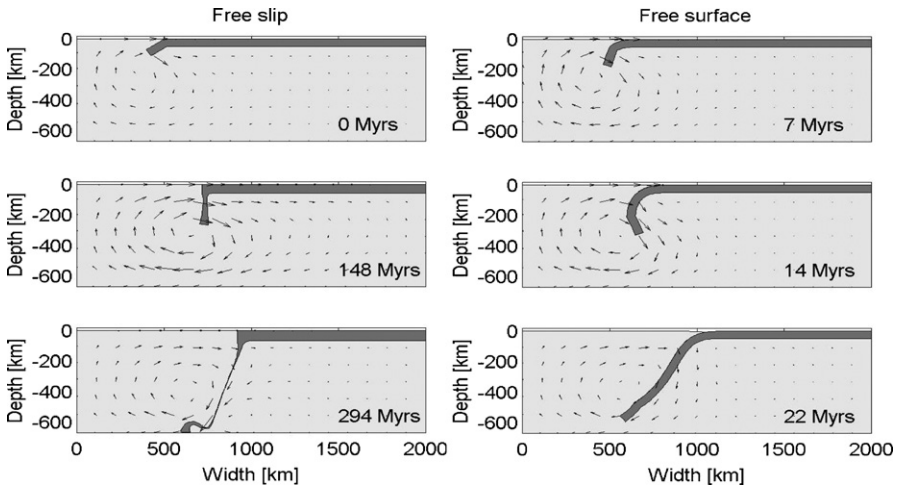

Fig. 1. Free subduction experiment in which a linear viscous slab sinks into a linear viscous mantle. The upper boundary condition is either free slip (left) or free surface (right). Clearly, the upper boundary condition has a significant effect on subduction dynamics, and only the free surface case is consistent with results of laboratory experiments. The average time step for the free surface case is significantly smaller than for the free surface case. Model parameters employed are: the slab has a density of $\rho = 3250\ kg/m^3$ and a viscosity of $\eta = 10^{23}$ Pa s, whereas the mantle has $\rho = 3200\ kg/m^3$, $\eta = 10^{20}$ Pa s, the initial slab was 50 km thick, 1500 km long, and has a 125 km long notch that initially subducted with an angle of 34°. Free slip conditions are applied on the lower and side boundaries, and gravitational acceleration was $9.81\ m/s^2$.

of ~800,000 years. For stability reasons, the free surface simulation had a time step restriction that limited the maximum vertical displacement to no more than 10 m during a single time step (and to no more than 10,000 years at any time). As a result, the average time step during this simulation was ~1300 years. Compared to cases with a free slip upper boundary condition, it is thus numerically very expensive to perform free surface simulations.

The numerical instabilities that develop if a too large time step is employed in combination with a free surface, can be illustrated with a Stokes-flow example, which is taken here as a lithospheric detachment in which a material of high density and viscosity moves downwards through an underlying mantle lithosphere of lower density and viscosity (Fig. 2A). If a constant time step of 2500 years is employed, the simulation evolves in a stable manner and

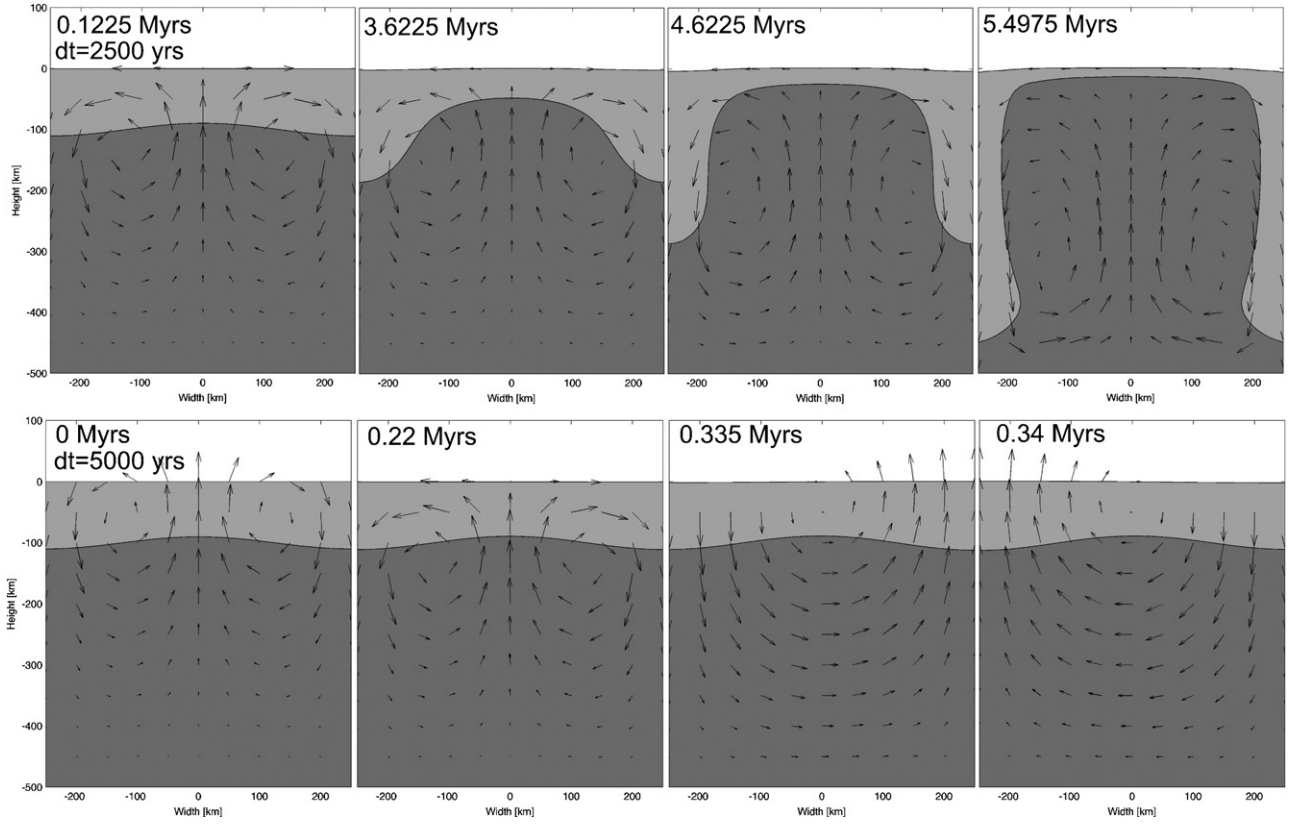

Fig. 2. Rayleigh–Taylor instability of a dense, more viscous layer ($\rho = 3300\ kg/m^3$, $\eta = 10^{21}$ Pa s), sinking through a less dense fluid ($\rho = 3200\ kg/m^3$, $\eta = 10^{20}$ Pa s). Side boundaries are free slip, the lower boundary is no-slip and the upper boundary is a free surface. The box is 500 × 500 km in size, and gravitational acceleration was $9.81\ m/s^2$. The initial perturbation was sinusoidal with initial amplitude of 5 km. A constant time step of 2500 years (A) or 5000 years (B) was employed, with Q_2P_{-1} quadrilateral elements and 51 × 51 nodes. Whereas the 2500 years simulation evolves smoothly, the simulation with $\Delta t = 5000$ years results in a sloshing instability, in which the velocity pattern changes direction from one time step to the other.

Please cite this article in press as: Kaus, B.J.P., et al., A stabilization algorithm for geodynamic numerical simulations with a free surface. Phys. Earth Planet. In. (2010), doi:10.1016/j.pepi.2010.04.007

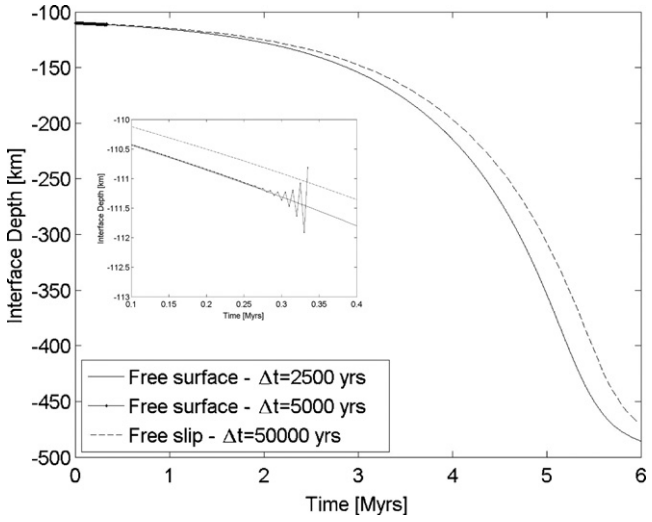

Fig. 3. Depth of the interface at $x = -250$ km versus time for the free surface simulations of Fig. 2. The inset shows that the simulation with constant Δt of 5000 years results in a numerical instability. For comparison we also show a simulation with a free slip upper boundary condition. In this case, a time step of $\Delta t = 50{,}000$ years could be employed without causing a numerical instability.

topography builds up gradually and decays with time once the high density material sinks to the bottom of the model box (Fig. 2A).

However, if the same simulation is performed with a constant time step of 5000 years an instability occurs which we term the "sloshing instability" or the "drunken sailor effect" (Y. Podladchikov, personal communication, 2000). Instead of dripping downwards (as the analytical solution would predict), the simulation develops an unphysical velocity field that flips direction from one time step to the other (Fig. 2B). Models in which the upper boundary is a free slip boundary, on the other hand, can be performed with a time step of 50,000 years without any evidence of numerical instabilities (Fig. 3).

Empirical experimentation indicates that the density contrast between rocks and air is the key parameter, which restricts the time step in these simulations. Typical densities of rocks are $\rho \sim 3000\,\mathrm{kg/m^3}$, whereas typical density differences between the lithosphere and mantle, which drive lithospheric-scale processes, are 30–100 $\mathrm{kg/m^3}$.

The driving force from the topography of the lithosphere-mantle interface is thus 30–100 times smaller than that of the air-rock interface. Since the stress σ, is proportional to $\sigma \propto \Delta\rho g A$, one can conclude that changing the surface topography A by one meter, induces stresses that are 30–100 times larger than those caused by moving the bottom of the lithosphere by 1 m. Using too large a time step might bring the topography out of isostatic equilibrium with the rest of the model, with a numerical instability as a result. Using higher-order time stepping algorithms, such as a fourth order Runga–Kutta algorithm (instead of the Eulerian time stepping method used in Fig. 1), does not improve the situation, since it essentially requires one to perform several explicit iteration steps during one time step. The system might come out of isostatic equilibrium during any of these iterations, which will yield non-physical results.

We observed that the above mentioned instability does not only occur during the initial stages of the model, but also during more evolved stages, particularly in cases with a subduction setup (Schmeling et al., 2008) or with erosion and lithospheric deformation (Kaus et al., 2008). A workaround is to limit the time step in such a manner that the changes in the topography are no more than 10–50 m per time step (for Earth-like densities). The resulting time steps, however, are very small, which makes the models computationally very expensive, particularly compared to free slip models.

Another potential solution to eliminate the instability is to combine a Lagrangian finite element method with a fully implicit time stepping algorithm, in which the nodal coordinates of a mesh are treated as additional degrees of freedom. The resulting system of equations, however, is considerably larger than the original Stokes problem. In addition, it becomes nonlinear and may require significantly more CPU time to solve than the original problem (e.g., Cuvelier et al., 1986). This can be solved by either using a Picard-type iteration approach (e.g., Nickell et al., 1974; Ramanan and Engelman, 1996) or by using a full Newton–Rhapson iteration scheme in which the stiffness matrix is recomputed in the new geometry (e.g., Cuvelier and Schulkes, 1990; Kistler and Scriven, 1984). Most existing research on free surface flows focuses on flows in which inertial terms or surface tension is relevant. Here we describe a different approach, appropriate for inertial-free geodynamic models, which requires only minor modifications to existing (FEM) velocity–pressure Stokes solvers, but which allows the use of significantly larger time steps, thereby providing a drastic reduction in the run time for free surface simulations.

2. Governing equations

In geodynamics, we commonly use the Boussinesq approximation, which assumes that rocks are incompressible on geological timescales, and for which the governing equations can be written as

$$D_{ii} = 0, \tag{1}$$

$$\sigma_{ij,j} = \rho g_i, \tag{2}$$

where $D_{ij} = 1/2(v_{i,j} + v_{j,i})$ is strain rate, v_i velocity, g_i gravitational acceleration, ρ density, x_i are the spatial Cartesian coordinates, $\sigma_{ij} = -P + \tau_{ij}$ stresses, $P = -(\sigma_{ii})/3$ pressure and τ_{ij} deviatoric stresses.

The rheology we use in this work is Newtonian viscous, which is given by

$$\tau_{ij} = 2\eta D_{ij}, \tag{3}$$

where η denotes viscosity. In general, the viscosity is a function of many parameters including temperature. Moreover, rheologies typically employed in lithospheric-scale geodynamic codes are visco-(elasto)-plastic rather than viscous. In this work, such additional complexities are ignored as a viscous free surface model is sufficient to illustrate the underlying problem. The methodology we propose can be directly applied to more complex rheologies, as well as to problems involving the energy equation.

In addition to the Stokes equations, an evolutionary equation is present which advects a material field Ψ according to

$$\Psi_{,t} + v_i \nabla \Psi = 0 \tag{4}$$

Eqs. (1)–(4) thus forms a system of four equations with four unknowns.

3. Numerical formulation

3.1. Classical weak formulation of the momentum equation

In most numerical codes employed in geodynamics, the mechanical Eqs. (1)–(3) are solved independently from material advection Eq. (4). The weak finite element formulation of the momentum Eq. (2) is obtained by multiplying the governing equations by a test function w_i and integrating it over the domain:

$$\int_V (\sigma_{ij,j} - \rho g_i) w_i dV = 0, \tag{5}$$

Please cite this article in press as: Kaus, B.J.P., et al., A stabilization algorithm for geodynamic numerical simulations with a free surface. Phys. Earth Planet. In. (2010), doi:10.1016/j.pepi.2010.04.007

which yields

$$\int_V (\sigma_{ij} w_{i,j} - \rho g_i w_i) dV - \int_\Gamma w_i t_i d\Gamma = 0, \quad (6)$$

where $t_i = \sigma_{ij} n_j$ is a given surface traction vector, n_j is the outward unit normal vector of the boundary $d\Gamma$, and the weight function w_i vanishes on those parts of the surface where velocities are prescribed.

3.2. Weak formulation with time-evolution

The numerical simulation of a fluid flow problem which includes the evolution of a Lagrangian free surface is nonlinear as the fluid velocity, pressure and coordinates defining the spatial discretizations are all unknown (Zienkiewicz and Taylor, 2000a,b). For economy, rather than solve the fully coupled nonlinear system, such problems are usually solved using a predictor step, followed by a number of correction steps which are designed to drive the system towards mechanical equilibrium (e.g., Cuvelier et al., 1986; van Keken, 1993). A critical factor affecting the accuracy of the predictor step is the choice of reference geometric state of the continuum (or reference configuration) used at the beginning of each time step. The reference configuration defines the geometric state from which all subsequent configurations are constructed. If we define the coordinates of our continuum by x_i, then one possible reference configuration for the subsequent time step is

$$x_i \to x_i + \Theta \Delta t v_i \quad (7)$$

where $0 \le \Theta \le 1$ and Δt is a small but finite time step.

A possible higher order, or tangent, formulation for the predictor step may be obtained by inserting Eq. (7) into the differential quotients included in Eq. (6) and expanding the result as a Taylor series, including only terms, which are linear in v_i. As a consequence, only the gravity force term in the virtual power expression in Eq. (6) is modified according to

$$\begin{aligned} &\int_{V(x_i+\Theta v_i \Delta t)} \rho g_i w_i dV \\ &\approx \int_{V(x_i)} [\rho g_i w_i + \Theta \Delta t (\rho g_i w_i)_{,k} v_k + \Theta \Delta t (\rho g_i w_i) v_{k,k}] dV + \cdots \\ &\approx \int_{V(x_i)} [\rho g_i w_i + \Theta \Delta t (\rho g_i w_i v_k)_{,k}] dV \end{aligned} \quad (8)$$

Applying Gauss theorem yields:

$$\begin{aligned} &\int_{V(x_i)} (\rho g_i w_i + \Theta \Delta t (\rho g_i w_i v_k)_{,k}) dV \\ &= \int_{V(x_i)} \rho g_i w_i dV + \int_{\Gamma(x_i)} \Theta \Delta t \rho g_i w_i v_n d\Gamma \end{aligned} \quad (9)$$

where the surface normal velocity is defined as $v_n = v_i n_i$. Inserting Eq. (9) into Eq. (6) yields the weak form of the boundary value problem for the predictor step at each time step:

$$\begin{aligned} &\int_{V(x_i+\Theta v_i \Delta t)} (\sigma_{ij} w_{i,j} - \rho g_i w_i) dV - \int_{\Gamma(x_i+\Theta v_i \Delta t)} w_i t_i d\Gamma \\ &\approx \int_{V(x_i)} (\sigma_{ij} w_{i,j} - \rho g_i w_i) dV \\ &- \int_{\Gamma(x_i+\Theta v_i \Delta t)} w_i (t_i + \Theta \Delta t \rho g_i v_n) d\Gamma = 0 \end{aligned} \quad (10)$$

or

$$\int_{V(x_i)} (\sigma_{ij} w_{i,j} - \rho g_i w_i) dV - \int_{\Gamma(x_i)} w_i (t_i + t_i^g) d\Gamma = 0 \quad (11)$$

where we have now introduced an additional boundary traction term $t_i^g = \int_\Gamma \Theta \Delta t \rho v_n g_i w_i d\Gamma$. In the special case that n_k = constant = (0, 0, 1) (i.e., slopes on the free surface are small), we obtain, $t_3^g = \Theta \Delta t \rho g v_3, \quad t_1^g = 0, \quad t_2^g = 0$.

3.3. Mixed finite element formulation

We solve Eq. (11), subject to the incompressibility constraint Eq. (1), using standard mixed finite elements. Accordingly, we split the total stress into a deviatoric part (τ_{ij}) and a pressure (p) via

$$\sigma_{ij} = \tau_{ij} - p \delta_{ij}$$

Employing this formulation, Eq. (11) becomes

$$\begin{aligned} &\int_V w_{i,j} \tau_{ij} dV - \int_V w_{i,j} p \delta_{ij} dV + \int_\Gamma w_i t_i^g d\Gamma \\ &= \int_V w_i (\rho g_i) dV + \int_\Gamma w_i t_i d\Gamma, \end{aligned} \quad (12)$$

with the weak incompressibility constraint

$$-\int_V q u_{i,i} dV = 0$$

In the above, w_i and q are suitably chosen test functions which vanish on the Dirichlet boundaries. We refer the reader to standard finite element textbooks (see, e.g., Cuvelier et al., 1986; Hughes, 1987) for a complete discussion of the weak formulation for incompressible Stokes flow and the admissible choices for (w_i, q).

The discrete problem is defined by sub-dividing the domain $\mathbf{\Omega}$ into a set of non-overlapping elements with domain $\mathbf{\Omega}^e$, and replacing the continuous test functions by piecewise defined functions over each element. We denote the discrete test functions via (N_i^v, N^p). We adopt the Galerkin formulation, thus our continuous unknowns (v_i, p) are approximated over each element via

$$\begin{aligned} \mathbf{v}(\mathbf{x}) &\approx \sum \mathbf{N}_k^v(\mathbf{x}) \mathbf{v}_e^k \\ p(\mathbf{x}) &\approx \sum N_k^p(\mathbf{x}) p_e^k \end{aligned}, \quad (13)$$

where ($\mathbf{v}_e^k$, p_e^k) are the nodal velocities and pressures associated with element e.

By introducing the discrete functions Eq. (13) into Eq. (12), the continuous problem can be written out in a matrix form, over each element, as

$$\begin{aligned} &\mathbf{K}_e \mathbf{v}_e + \mathbf{G}_e \mathbf{p}_e + \mathbf{L}_e \mathbf{v}_e = \mathbf{F}_e \\ &\mathbf{G}_e^T \mathbf{v}_e = 0 \end{aligned} \quad (14)$$

The discrete operators $\mathbf{K}_e, \mathbf{G}_e, \mathbf{F}_e$ are standard finite element stiffness matrices, however for completeness we present them below

$$\begin{aligned} \mathbf{K}_e &= \int_{\Omega^e} \mathbf{B}^T \mathbf{D} \mathbf{B} dV \\ \mathbf{G}_e &= -\int_{\Omega^e} \mathbf{B}^T \mathbf{m} N_p dV \\ \mathbf{F}_e &= \int_{\Omega^e} \mathbf{N}^v (\rho \mathbf{g}) dV + \int_{\Gamma^e} \mathbf{N}^v \mathbf{t} d\Gamma \end{aligned} \quad (15)$$

The traction introduced by the time-discretization $\mathbf{L}_e$, is given by

$$\mathbf{L}_e = \int_{\Gamma^e} \mathbf{N}^v (\Theta \rho \Delta t \mathbf{g}) \mathbf{n} d\Gamma.$$

Please cite this article in press as: Kaus, B.J.P., et al., A stabilization algorithm for geodynamic numerical simulations with a free surface. Phys. Earth Planet. In. (2010), doi:10.1016/j.pepi.2010.04.007

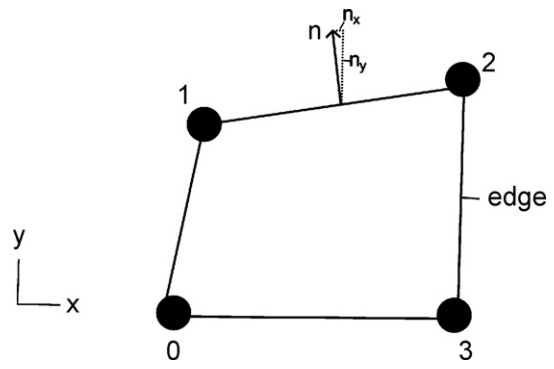

Fig. 4. Two-dimensional linear quadratic element with outward pointing normal vector.

Since $\mathbf{L}_e$ depends on velocity, we can write the system of equations as

$$\begin{pmatrix} \tilde{\mathbf{K}}_e & \mathbf{G}_e \\ \mathbf{G}_e^{\mathbf{T}} & 0 \end{pmatrix} \begin{pmatrix} \mathbf{v}_e \\ \mathbf{p}_e \end{pmatrix} = \begin{pmatrix} \mathbf{F}_e \\ 0 \end{pmatrix} \tag{16}$$

where

$$\tilde{\mathbf{K}}_e = \mathbf{K}_e + \mathbf{L}_e$$

Obviously, $\mathbf{L}_e = 0$ if $\Theta = 0$ (and we recover the "classical" Stokes equations).

We now discuss how to evaluate the stabilizing traction boundary integral $\mathbf{L}_e$. In finite element analysis, the evaluation of surface integrals is typically performed by only integrating along the edges of the elements, which form part of the boundary of the domain $\boldsymbol{\Omega}$. This is appropriate as the surface integrals along the element edges interior to $\boldsymbol{\Omega}$ will all cancel, leaving behind only the contribution from element edges which are not shared by any other element. In this work, we perform the surface integrals over *every* edge of the element domain $\boldsymbol{\Omega}^e$. We prefer this approach as (i) the computational cost of evaluating the additional surface integrals on the element edges is comparable to evaluating the stiffness matrix $\mathbf{K}$, both of which are negligible compared to time taken to perform the solve and (ii) including the interior element edges will naturally incorporate any *internal* density interfaces within the domain $\boldsymbol{\Omega}$, in addition to the density jump at the free surface. In regions where two elements possess a shared boundary with matching densities on either side, the surface integral contributions from each element will cancel. Conversely, if the neighbouring elements possess different densities, then the surface integrals will not cancel and the correct stabilizing contribution will be introduced.

3.4. Implementation aspects

In the above, we represented the discrete part of the problem associated with stabilizing surface integral as an element stiffness matrix. This choice was partially for notation simplicity and partially because we wish to evaluate the surface integral along all of the element edges. In addition, it is computationally convenient to perform an element-based assembly as this is consistent with the finite element framework of assembling element stiffness matrices. The non-zero structure of the element stiffness matrix of such a procedure is described below. Consider the 2D, four node quadrilateral element shown in Fig. 4. We will assume that the element-nodal velocity unknowns are ordered according to

$$\mathbf{v}_e = (v_0^x, v_0^y, v_1^x, v_1^y, v_2^x, v_2^y, v_3^x, v_3^y). \tag{17}$$

Using this ordering and the node numbering shown in Fig. 4, and if we include all the element edges in the surface integral, we will obtain a matrix with the following non-zero structure

$$\mathbf{L}_e = \begin{pmatrix} X & X & X & X & & & X & X \\ X & X & X & X & & & X & X \\ X & X & Y & Y & Y & Y & & \\ X & X & Y & Y & Y & Y & & \\ & & Y & Y & Y & Y & X & X \\ & & Y & Y & Y & Y & X & X \\ X & X & & & X & X & X & X \\ X & X & & & X & X & X & X \end{pmatrix} \tag{18}$$

For each edge E of an element e, we can explicitly define the traction contribution (in 2D) as

$$\hat{\mathbf{L}}^E = \begin{pmatrix} \int_{\Gamma^e} \Delta t \rho g_x n_x N_i^v N_j^v dS & \int_{\Gamma^e} \Delta t \rho g_x n_y N_i^v N_j^v dS \\ \int_{\Gamma^e} \Delta t \rho g_y n_x N_i^v N_j^v dS & \int_{\Gamma^e} \Delta t \rho g_y n_y N_i^v N_j^v dS \end{pmatrix} \tag{19}$$

The indices i,j are determined by the edge index E (see Fig. 4).

The complete traction term defined over the entire element is computed by performing the typically finite element summation, i.e.

$$\mathbf{L}_e = \sum^{\text{all edges}} \hat{\mathbf{L}}^E. \tag{20}$$

To contrast with the classical FE approach, if we let the edge defined by nodes 1 and 2 (from Fig. 4) denote an interface and we only integrated along this surface, than the only non-zero entries in $\mathbf{L}_e$ will those denoted by Y in Eq. (18). Using the same free surface example, and assuming we only wish to incorporate corrections from the density jump at the free surface, the special case (in 2D), when $n_k = \text{constant} = (0, 1)$ will yield $t_2 = -(\rho g_y \Delta t) v^y, \quad t_1 = 0$. The corresponding edge correction matrix is given by

$$\hat{\mathbf{L}}^E = \begin{pmatrix} 0 & 0 \\ 0 & \int_{\Gamma^e} \Delta t \rho g_y n_y N_i^v N_j^v dS \end{pmatrix} \tag{21}$$

If the non-zero entry was approximated via nodal integration, then the resulting element traction correction matrix would be

$$\mathbf{L}_e \approx \tilde{\mathbf{L}}_e = \text{diag}(\,0 \quad 0 \quad 0 \quad T \quad 0 \quad T \quad 0 \quad 0\,) \tag{22}$$

where

$$T = \frac{1}{2} \Delta t \rho g_y n_y \Delta L$$

where ΔL is the length of the edge segment.

Note that in general, each element stiffness matrix $\hat{\mathbf{L}}^E$ will be non-symmetric. This is an immediate consequence of the fact that the terms $g_x n_y$ and $g_y n_x$ will generally not be equal. For a simulation in which the fluid possesses a single density and a free surface, all the surface integrals performed over the shared element faces will exactly cancel. Only the entries associated with the boundary nodes along the free surface will produce non-symmetric entries in $\tilde{\mathbf{K}}$. Preserving the symmetry of the discrete problem is potentially advantageous for both factorization techniques and preconditioned iterative methods, which are used to solve the matrix problem. We consider two methods to evaluate $\hat{\mathbf{L}}^E$:

(I) Use Gauss–Lobatto quadrature to evaluate the full matrix $\hat{\mathbf{L}}^E$, in which the integration points are located at the nodal points. We will call this the free surface stabilization algorithm 1 (FSSA 1). This algorithm does typically not yield a symmetric system of equations.
(II) Use a "lumped" version of $\hat{\mathbf{L}}^E$, where rather than using the full matrix, the diagonal version of $\hat{\mathbf{L}}^E$ is used in combination with

Gauss–Legendre quadrature and off-diagonal terms are set to zero. This results in a symmetric system of equations (FSSA 2).

In Section 4, we illustrate via a number of numerical examples that both choices produce stable numerical results, and that the (numerically faster) FSSA2 method yields very similar results as the FSSA1 method.

From an implementation point of view, the only modification to the classical Stokes equations consists of evaluating $\mathbf{L}_e$ and adding it to the standard element stiffness matrix $\mathbf{K}_e$.

After assembling the element stiffness matrixes, the global stiffness matrix becomes

$$\begin{pmatrix} \tilde{\mathbf{K}} & \mathbf{G} \\ \mathbf{G}^T & 0 \end{pmatrix} \begin{pmatrix} \mathbf{V} \\ \mathbf{p} \end{pmatrix} = \begin{pmatrix} \mathbf{F} \\ 0 \end{pmatrix} \tag{23}$$

where $\tilde{\mathbf{K}}$ is the global stiffness matrix, formed by summing $\tilde{\mathbf{K}}_e$, $\mathbf{G}$ the discrete gradient operator, and $\mathbf{F}$ contains terms related to the body forces and the prescribed tractions.

4. Results

We have implemented the approach described in Section 3 within MILAMIN_VEP, which is a two-dimensional geodynamic modelling code that is based on the fast MATLAB-based Stokes solver MILAMIN (Dabrowski et al., 2008) but include remeshing, visco-elasto-plastic rheologies as well as a tracer-based method to advect material properties (Kaus, 2009; Kaus et al., 2009). MILAMIN_VEP works both for triangular unstructured and quadrilateral structured meshes. Here, we employ both 7-node triangular elements (T_2P_{-1}) with discontinuous pressures, as well as Q_2P_{-1} quadrilateral elements.

Here we illustrate the potential of our method with two geodynamically relevant examples, and discuss the optimal choice of Θ.

4.1. Free surface Rayleigh–Taylor test

The RT test described in the introduction (Fig. 2) was repeated here with two different time stepping criteria. The first employs a constant time step Δt, whereas the second uses a Courant criteria given by

$$\Delta t = C \frac{\min(\Delta \Gamma^e)}{\max(v_x, v_z)}$$

where $\Delta \Gamma^e$ indicates the edge length of an element and v_x, v_z vertical and horizontal velocities. If neither stabilization (FSSA1 or FSSA2) is employed, the maximum time step that gives stable results is $\Delta t = 2500$ years or $C = 0.003$ for the two time step criteria respectively. The models initially closely follow the results of a thick plate semi-analytical solution (which is described in more detail in Kaus and Becker, 2007), but deviate from this after the layer has thickened to ~150 km (which is to be expected as the analytical solution is only valid for small amplitudes).

If the FSSA2 is employed (with $\Theta = 0.5$), however, it is possible to use time steps of $\Delta t = 50{,}000$ years or $C = 0.5$, with nearly identical results (Fig. 5).

In order to better understand the accuracy of the method we have performed a series of systematic calculations to understand (1) the accuracy of our (Eulerian) time stepping algorithm, (2) the accuracy of FSSA1 versus FSSA2, and (3) the effect of varying Θ.

The accuracy of the time stepping algorithm can be tested with simulations in which the upper boundary condition is free slip, since these simulations are numerically stable even if the FSSA algorithm is not employed ($\Theta = 0$). In order to compare the various results, we measured the interface depth after 3 Myrs, and compare the results with the smallest time step simulation with

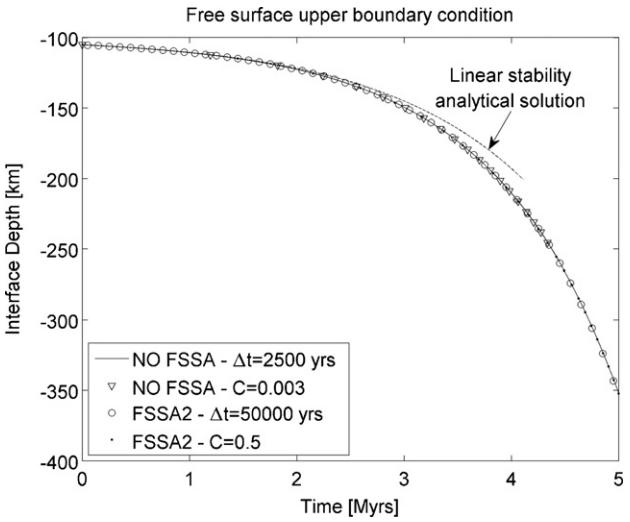

Fig. 5. Comparison of free surface simulations with and without the free surface stabilization algorithm. If the FSSA is not employed, the maximum time step for stable calculations is 2500 years (if constant Δt is employed), or $C = 0.003$ (if a Courant-based time step criteria is used). With the FSSA (with $\Theta = 0.5$), a time step that is 20–167 times larger can be employed, giving nearly identical overall results.

$\Theta = 0$. Results indicate that using a time step of 50,000 years gives an error of around 1%, whereas the error is larger if a Courant criterion of $C = 1$ is used (Fig. 6). If we employ the FSSA with $\Theta = 1$ the errors are very similar, but with opposite sign. Very small differences occur between simulations that use the FSSA1 and ones that use the FSSA2. Simulations with $\Theta = 0.5$, however, are significantly more accurate and within a percent of the 'true' solution even for the largest tested time steps (Fig. 6). If the time step is further increased, we found that simulations with $\Theta = 0.5$ ultimately become numerically unstable, whereas simulations with $\Theta = 1$ are stable for a somewhat larger range of time steps.

We have repeated these experiments for a setup with a free surface upper boundary. The results are essentially the same, with little differences between FSSA1/FSSA2 and $\Theta = 0.5$ yielding the most accurate results (Fig. 7).

The 'optimal' value of $\Theta = 0.5$ can be interpreted as using half the 'old' and half the 'new' position of the density interface. Interestingly, the results that are obtained with $\Theta = 0.5$ are significantly more accurate than results of simulations that do not employ the FSSA ($\Theta = 0$).

4.2. Free subduction

The second setup comes from a benchmark study of Schmeling et al. (2008) in which an attempt was made to reproduce laboratory experiments of free subduction. In these laboratory studies, a slab of high density and higher viscosity was placed in a tank of lower density and viscosity. A range of numerical codes used a setup that was inspired from the laboratory experiment (Fig. 8A), and that employed either a 'true' free surface or that mimicked the free surface with a 'sticky air' layer. It was found that the presence of the (pseudo) free surface is important in these simulations, and reasonable agreement between various codes was obtained for the setup of Fig. 8. As described above, however, the presence of the free surface poses severe time step restrictions and some of the codes therefore required days to weeks of CPU time. This is clearly unsatisfying if one wants to study the dynamics of subduction in a more systematic manner.

Here we therefore repeat the experiment with MILAMIN_VEP, and test the potential of the FSSA for this setup. Rather than using a regular numerical grid (as in the Rayleigh–Taylor example), we

Please cite this article in press as: Kaus, B.J.P., et al., A stabilization algorithm for geodynamic numerical simulations with a free surface. Phys. Earth Planet. In. (2010), doi:10.1016/j.pepi.2010.04.007

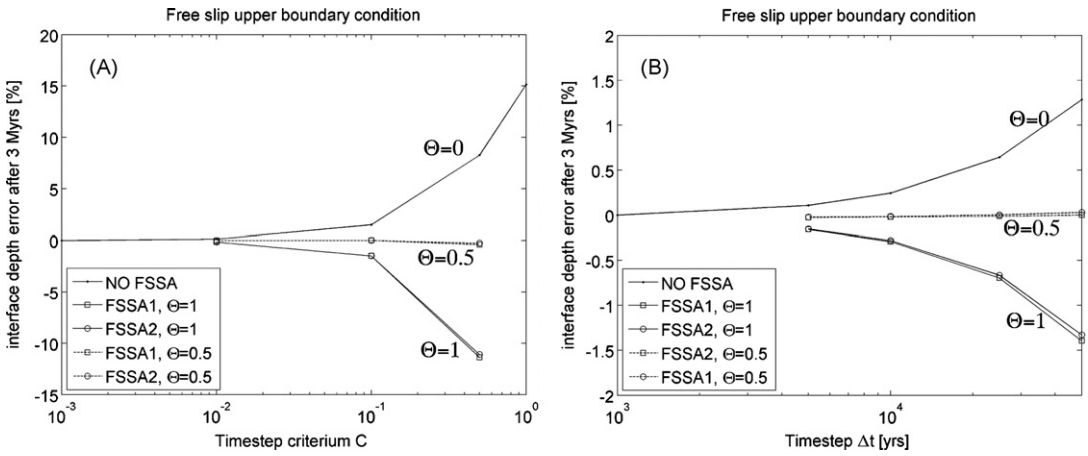

Fig. 6. Effect of time step algorithm, time step size and FSSA algorithm on geometry error in simulations with a free slip upper boundary condition. The geometry error is the difference of the maximum depth of the interface to the simulation with smallest time step and no FSSA ($\Theta = 0$). Clearly, the employed value of Θ has a large effect on the accuracy. Cases with FSSA and $\Theta = 1$ have a similar error convergence as cases without FSSA (although the sign is different). Cases with $\Theta = 0.5$, on the other hand, are significantly more even for large time steps. There is little difference between FSSA1 and FSSA2.

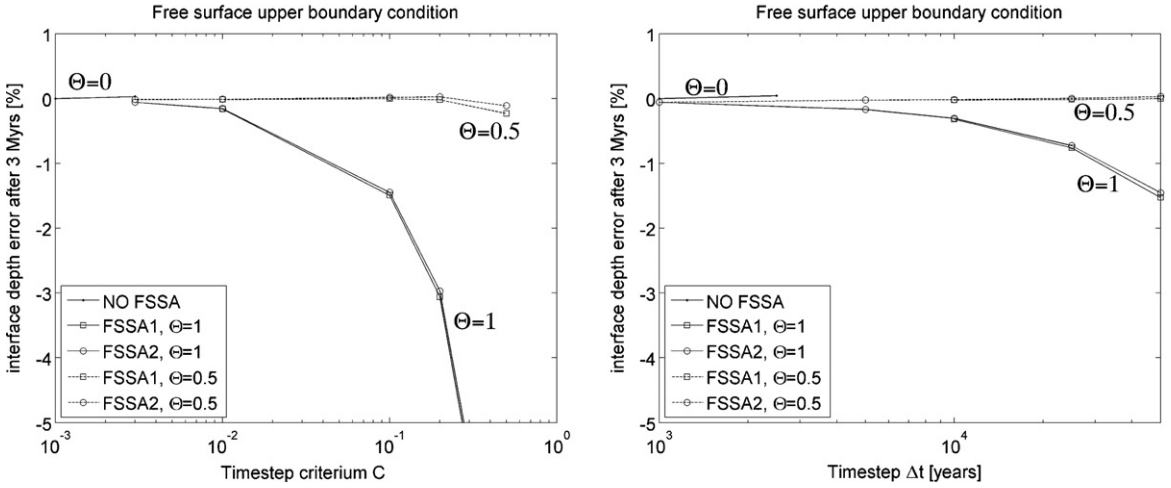

Fig. 7. As in Fig. 6, but with a free surface upper boundary condition. Cases without FSSA are numerically unstable for larger time steps; only the stable results are plotted. As in the free slip runs, there is little difference between the particular implementation of the FSSA, but the choice of Θ does have a significant effect, with $\Theta = 0.5$ yielding the most accurate results.

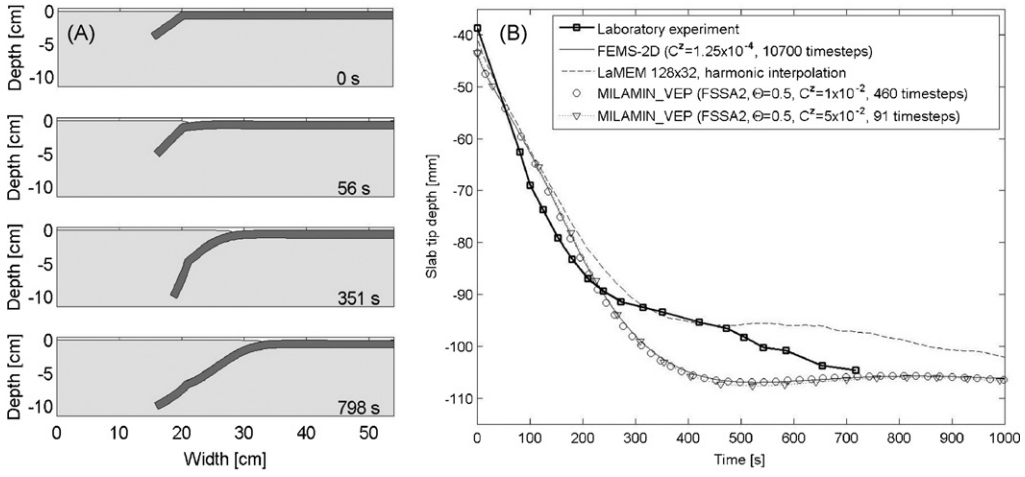

Fig. 8. (A) Temporal evolution of a subduction experiment, designed to mimic laboratory experiments of free subduction. The slab has $\rho = 1495\ \mathrm{kg/m^3}$ and $\eta = 3.5 \times 10^5\ \mathrm{Pa\,s}$, whereas the mantle has $\rho = 1415\ \mathrm{kg/m^3}$ and $\eta = 32\ \mathrm{Pa\,s}$. Free slip boundary conditions are applied everywhere except at the top boundary, which is a free surface. An unstructured triangular mesh is used for these simulations with 7-node T_2P_{-1} shape functions. Results are in excellent agreement with a published subduction benchmark as well as with laboratory experiments (Schmeling et al., 2008). (B) Slab-tip depth versus time for various time stepping algorithms. Also shown are the results of a laboratory experiment as well as the results of FEMS-2D (which uses a different remeshing algorithm at the trench) and LaMEM (which is a FEM code with a structured mesh). Clearly, the FSSA allows the use of significantly larger time steps with similar overall accuracy.

Please cite this article in press as: Kaus, B.J.P., et al., A stabilization algorithm for geodynamic numerical simulations with a free surface. Phys. Earth Planet. In. (2010), doi:10.1016/j.pepi.2010.04.007

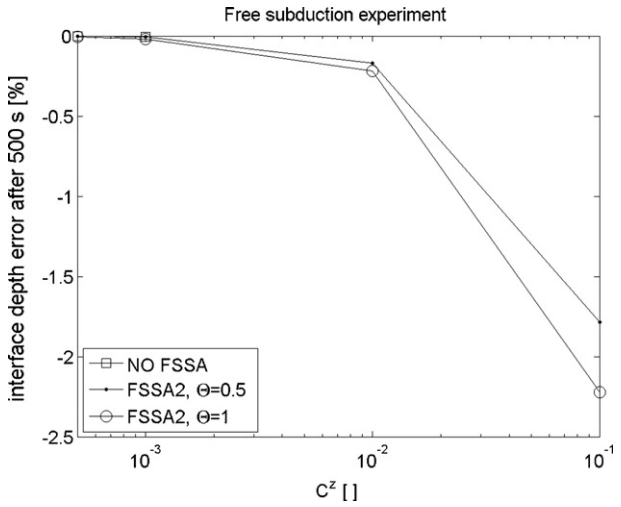

Fig. 9. Error of time stepping algorithms for the free subduction experiment. If the FSSA is not used, the maximum C^z that can be employed is $\sim 10^{-3}$, which shows that the FSSA significantly increases the time steps that can be employed with this setup. As in the Rayleigh–Taylor test, $\Theta = 0.5$ yields more accurate results, although the difference is less pronounced.

employ triangular elements with quadratic velocity and linear, discontinuous, pressure shape functions. The slab and the free surface are described by a marker chain and a finite element mesh is created from these chains with the help of the open-source code Triangle (Shewchuk, 2002). During a simulation, the mantle rolls on top of the subducting slab, which requires remeshing. An accurate treatment of the triple point was found to be important in such situations (Schmeling et al., 2008). Here we use an algorithm which kinematically moves mantle material on top of the subducting plate once a critical angle is exceeded. The new trench location is determined in a mass-conserving manner. In Schmeling et al., we have tested a number of different remeshing algorithms (including a non mass-conserving kinematic algorithm, which simply moved the trench position to the next node on the slab marker chain), and we found that little overall differences occur as long as the trench region is numerically well-resolved. The specific algorithm used here is similar to that used by the code FEMS-2D (which is also an unstructured FEM code), but it was improved to deal with cases in which the mantle forms overhangs (which might occur during very large time steps). Remeshing was performed every 5th time step or as soon as a critical trench angle of 20° was exceeded (which in many cases resulted in a remeshing step at each time step).

In these simulations the size of the elements might vary significantly between various regions of the model domain as well as between different time steps. A purely Courant-based time stepping criteria (which uses element edges as a length scale) therefore results in rapidly changing Δt between different time steps, depending on whether remeshing resulted in small elements or not. We therefore here use a different criteria which takes the height of the model domain H as characteristic length scale,

$$\Delta t = C^z \frac{H}{\max(v_x, v_z)}$$

Results (Fig. 8B) show that by using FSSA we can speedup the simulations by a factor 100 whilst still achieving very similar results. Also shown are the results of FEMS-2D (which are reproduced quite closely), as well as the results of the laboratory experiment and that of a structured finite element code (LaMEM).

A convergence test, which measured slab-tip depth after 500 s, showed that ~2% error is introduced by increasing C^z from 5×10^{-4} to 0.1 (Fig. 9). Simulations with $\Theta = 0.5$ are more accurate than simulations with $\Theta = 1$, but the differences are less pronounced than in the Rayleigh–Taylor experiment.

5. Discussion and conclusions

Geodynamics numerical simulations in which a free surface is present can be numerically challenging, particularly if the lower part of the model box consists of a weaker material (e.g., the lithosphere). One of the problems is that the time step in such models has to be very small compared to similar models with a free slip upper boundary condition, otherwise a sloshing instability will occur.

Here, we describe a numerical algorithm that largely overcomes this issue. The algorithm is based on an extension of the force balance equations to take into account the effect that the numerical grid deforms from one time step to the other. By making an expansion on the body force, one obtains an additional surface traction term, which can be numerically integrated over every element and which is essentially proportional to density jumps between adjacent elements. We explored two different finite element numerical implementations of this free surface stabilization approach (FSSA), and found that the easiest to implement algorithm (FSSA2) gives nearly identical results to the more general method. If the FSSA is employed, the stable time step which can be used within a simulation can be increased by up to two orders of magnitude compared to simulations without the FSSA.

Although we have not explored this here, we expect that the FSSA will also stabilize Eulerian numerical codes that employ a 'sticky air' free surface (as the algorithm is sensitive to jumps in density). Moreover, it should in principle be possible to extend the algorithm to Eulerian finite difference codes, although an accurate tracking of the free surface will be crucial here.

Acknowledgements

We thank the editor Mark Jellinek and reviewers Jeroen van Hunen and Jean Braun for constructive comments.

References

Braun, J., 2006. Recent advances and current problems in modelling surface processes and their interactions with tectonics and crustal deformation. In: Buiter, S.J.H., Schreurs, G. (Eds.), Analog and Numerical Modelling of Crustal-scale Processes. Special Publication of the Geological Society of London, pp. 307–325.
Braun, J., Yamato, P., in press. Structural evolution of a three-dimensional, finite-width crustal wedge. Tectonophysics.
Cuvelier, C., Schulkes, R.M.S.M., 1990. Some numerical-methods for the computation of capillary free boundaries governed by the Navier–Stokes equations. SIAM Review 32 (3), 355–423.
Cuvelier, C., Segal, A., van Steemhoven, A.A., 1986. Finite Element Methods and Navier–Stokes Equations. Mathematics and its applications. Reidel Publishing company, Dordrecht, p. 483.
Dabrowski, M., Krotkiewski, M., Schmid, D.W., 2008. MILAMIN: MATLAB-based FEM solver for large problems. Geochemistry Geophysics Geosystems, doi:10.1029/2007GC001719.
Gurnis, M., Eloy, C., Zhong, S., 1996. Free-surface formulation of mantle convection. II. Implications for subduction zone observables. Geophysical Journal International 127, 719–727.
Hughes, T.J.R., 1987. The Finite Element Method. Dover Publications, New York.
Kaus, B.J.P., 2009. Factors that control the angle of shear bands in geodynamic numerical models of brittle deformation. Tectonophysics, doi:10.1016/j.tecto.2009.08.042.
Kaus, B.J.P., Becker, T.W., 2007. Effects of elasticity on the Rayleigh–Taylor instability: implications for large-scale geodynamics. Geophysical Journal International 168 (2), 843–862.
Kaus, B.J.P., Liu, Y., Becker, T.W., Yuen, D.A., Shi, Y.L., 2009. Lithospheric stress-states predicted from long-term tectonic models: influence of rheology and possible application to Taiwan. Journal of Asian Earth Sciences 36 (1), 119–134.
Kaus, B.J.P., Steedman, C.E., Becker, T.W., 2008. From passive continental margin to mountain belt: insights from analytical and numerical models and application to Taiwan. Physics of the Earth and Planetary Interiors 171 (1–4), 235–251.
Kistler, S.F., Scriven, L.E., 1984. Coating flow theory by finite-element and asymptotic analysis of the Navier–Stokes system. International Journal for Numerical Methods in Fluids 4 (3), 207–229.

Nickell, R.E., Tanner, R.I., Caswell, B., 1974. Solution of viscous incompressible jet and free-surface flows using finite-element methods. Journal of Fluid Mechanics 65 (August), 189–206.
Poliakov, A., Podladchikov, Y., 1992. Diapirism and topography. Geophysical Journal International 109, 553–564.
Ramanan, N., Engelman, M.S., 1996. An algorithm for simulation of steady free surface flows. International Journal for Numerical Methods in Fluids 22 (2), 103–120.
Schmeling, H., et al., 2008. A benchmark comparison of spontaneous subduction models—towards a free surface. Physics of the Earth and Planetary Interiors 171 (1–4), 198–223.
Shewchuk, J.R., 2002. Delaunay refinement algorithms for triangular mesh generation. Computational Geometry-Theory and Applications 22 (1–3), 21–74.
Simpson, G.D.H., 2006. Modelling interactions between fold-thrust belt deformation, foreland flexure and surface mass transport. Basin Research 18 (2), 125–143.
van Keken, P.E., 1993. Numerical modeling of thermochemically driven fluid flow with non-Newtonian theology. PhD Thesis. Utrecht University, Utrecht.
Willett, S.D., 1999. Orogeny and orography: the effects of erosion on the structure of mountain belts. Journal of Geophysical Research-Solid Earth 104 (B12), 28957–28981.
Zhong, S.J., Gurnis, M., Moresi, L., 1996. Free-surface formulation of mantle convection. 1. Basic theory and application to plumes. Geophysical Journal International 127 (3), 708–718.
Zienkiewicz, O.C., Taylor, R.L., 2000a. The Finite Element Method, Vol. 2, Solid Mechanics. McGraw Hill Book Company, London.
Zienkiewicz, O.C., Taylor, R.L., 2000b. The Finite Element Method, Vol. 3, Fluid Mechanics. McGraw Hill Book Company, London.

Please cite this article in press as: Kaus, B.J.P., et al., A stabilization algorithm for geodynamic numerical simulations with a free surface. Phys. Earth Planet. In. (2010), doi:10.1016/j.pepi.2010.04.007